Numerical Modeling Describing the Effects of Heterogeneous Distributions of Asperities on the Quasi-static Evolution of Frictional Slip

- Authors
- Authors and affiliations

- P. A. Selvadurai
- J. M. Parker
- S. D. Glaser

- o
- o
- o

1. 1.
2. 2.

Original Paper
First Online: 10 October 2017

Abstract

A better understanding of how slip accumulates along faults and its relation to the breakdown of shear stress is beneficial to many engineering disciplines, such as, hydraulic fracture and understanding induced seismicity (among others). Asperities forming along a preexisting fault resist the relative motion of the two sides of the interface and occur due to the interaction of the surface topographies. Here, we employ a finite element model to simulate circular partial slip asperities along a nominally flat frictional interface. Shear behavior of our partial slip asperity model closely matched the theory described by Cattaneo. The asperity model was employed to simulate a small section of an experimental fault formed between two bodies of polymethyl methacrylate, which consisted of multiple asperities whose location and sizes were directly measured using a pressure sensitive film. The quasi-static shear behavior of the interface was modeled for cyclical loading conditions, and the frictional dissipation (hysteresis) was normal stress dependent. We further our understanding by synthetically modeling lognormal size distributions of asperities that were randomly

distributed in space. Synthetic distributions conserved the real contact area and aspects of the size distributions from the experimental case, allowing us to compare the constitutive behaviors based solely on spacing effects. Traction-slip behavior of the experimental interface appears to be considerably affected by spatial clustering of asperities that was not present in the randomly spaced, synthetic asperity distributions. Estimates of bulk interfacial shear stiffness were determined from the constitutive traction-slip behavior and were comparable to the theoretical estimates of multi-contact interfaces with non-interacting asperities.

Keywords

Frictional faulting Contact mechanics Partial slip asperities Heterogeneous cohesive zone Traction-slip behavior

1 Introduction

Earthquakes and faulting in nature are not well understood but have been modeled as the coming together of two rough surfaces in which their contact points (asperities) dictate the relative frictional motion (Aki 1967; Scholz 2002). The study of friction and faulting, i.e., the coming together and subsequent rubbing of two rough surfaces, stems from the fields of contact mechanics (Hertz 1882; Mindlin 1949; Greenwood and Williamson 1966; Johnson 1985) and tribology (Archard 1953, 1957; Persson 1999, 2006), respectively. These fields have provided a framework to characterize stress concentrations formed at the asperity contact points that result in stress concentrations and a heterogeneous distribution of frictional properties. Understanding the nature of these stress concentrations is important due to the high-dependency of friction on normal stress (Dieterich and Kilgore 1996). At large scales, the residual stress fields caused by the asperities control the slip distribution (Hansen et al. 2000; Peyrat et al. 2004; Schmittbuhl et al. 2006) and likely dictate the evolution of friction during the inter-seismic and seismic phases of the earthquake cycle. Developing a better understanding of asperities and their constitutive (slip-traction) behavior during inter-seismic periods will allow for better estimates of seismic hazard during a wide variety of faulting scenarios, e.g., the variable increase in premonitory slip associated with earthquake nucleation sequences (Ohnaka 1992; Brodsky and Lay 2014; Kato et al. 2014, 2016; Obara and Kato 2016).

2 Nucleation Theory

Nucleation theory governs the behavior of the fault interface as it evolves from fully stuck, then through a period of stable creeping, to an unstable failure with rapid slip. The stress waves generated by unstable sliding of a

large fault area or on locally contacting asperities are recorded as earthquake signals. During earthquake nucleation, a frictional fault bears many similarities to an expanding shear fracture/crack (see Fig. 1a), which provides a basis for mathematical modeling (Scholz 2002).

Here we model the frictional fault in a body (volume V in Fig. 1a) as a localized planar discontinuity with a sparse population of small contacting areas referred to as asperities. The relative displacement across this planar discontinuity is referred to as fault slip $\delta\delta$, which accrues within the expanding shear crack as we apply shear tractions or displacement boundary conditions to the body. According to frictional stability theory (Rice and Ruina 1983), stable crack growth occurs until a critical crack half-length L_cLc after which an instability forms and the crack proceeds to grow dynamically. The constitutive relationship between applied shear traction and resultant slip accumulation on a frictional fault is not fully understood, although a handful of relationships have been proposed based on phenomenological observations from laboratory experiments. Predominantly cited are the slip-weakening (also known as slip-dependent) (Andrews 1976; Ida 1973; Ohnaka 1992) and rate- and state-dependent (RS) constitutive laws (Dieterich 1979; Ruina 1983; Rubin and Ampuer 2005). These relationships dictate the size, stress states and growth rate of the expanding shear rupture/crack and, therefore, determine when the frictional instability will form.

Mathematically, the ideal crack solution (Griffith 1921; Andrews 1976) has a stress singularity (concentration) at the crack tip. The cohesive zone was introduced to account for this unrealistic condition since real materials cannot sustain infinite stress (Ida 1972, 1973). In this cohesive region, shear stress breakdown was assumed to smoothly dissipate based primarily on phenomenological observations of laboratory experiments (Okubo and Dieterich 1984; Ohnaka and Yamashita 1989; Ohnaka and Shen 1999; McLaskey and Kilgore 2013; Svetlizky and Fineberg 2014). Typically, these models consist of homogenous stress states ahead and behind the crack tip. Recent improvement in the laboratory instrumentation—specifically the deployment of piezoelectric sensors (PZT)—is finding that during stress breakdown and stable rupture growth, there exists localized, high-frequency energy release [known as acoustic emissions (AEs)] that emanates along the fault and from within the nucleation region (McLaskey and Kilgore 2013; Selvadurai and Glaser 2015a). AEs were found to be the sudden failure of spatially discrete strength heterogeneities (i.e., asperities) (Selvadurai and Glaser 2014) and were precursors to the larger main shock. Multiple mechanisms have been proposed to explain why they occur, e.g., accelerated slip rates (McLaskey and Kilgore 2013) or length scale-dependent critical slip distances (Selvadurai and Glaser 2017). The notion of strength heterogeneities within an expanding shear rupture has been

proposed by Ohnaka (see Fig. 12 in Ohnaka 1992) and offers an explanation to foreshocks along natural faults (Ohnaka 1993; Jones and Molnar 1979; Brodsky and Lay 2014; Kato et al. 2014). It is likely that treating the stress breakdown across the crack tip's cohesive zone as smooth may not allow for some of the precursory phenomena observed in nature, such as foreshocks.

The model shown in Fig. 1a attempts to provide a framework to explain foreshocks by directly incorporating asperities. Two zones are defined within the expanding shear crack: (1) an orange region where shear stress along the discontinuity has been reduced to a residual level τ_r and (2) a breakdown (gray) region where shear stress is reduced from a peak level τ_p to that residual level. Stuck and partially stuck asperities are located in the breakdown/cohesive region (Ida 1972; Andrews 1976) and are believed to cause local strength heterogeneity (Ohnaka 1992, 1993). Figure 1b depicts an idealized shear stress (red) and slip accumulation (green) in the breakdown region emphasizing small perturbations at asperity contacts as proposed by Ohnaka (1992). By focusing on the behavior of a shear rupture front as it expands into a resistive patch of asperities (Fig. 1d), we seek to better understand the constitutive relationship and mechanisms governing stress breakdown near the crack tip.

To study the behavior of the cohesive zone, we imposed strength heterogeneity along the interface. Recent attempts to embed geologic heterogeneity into the RS framework (Ariyoshi et al. 2009, 2012; Dublanchet et al. 2013; Noda et al. 2013) have started to reveal the complexity of stresses near the crack tip. However, the distributions of strength and choice of material parameters in the models of these studies have been somewhat arbitrary. Incorporation of contact mechanics studies considering the stress field produced by the interaction of two rough surfaces (Archard 1961; Greenwood and Williamson 1966; Johnson 1985; Yoshioka 1997; Persson 2006; Paggi et al. 2014) could help to model the non-uniform stress field, due to geologic heterogeneities, in a more realistic manner.

Open image in new window

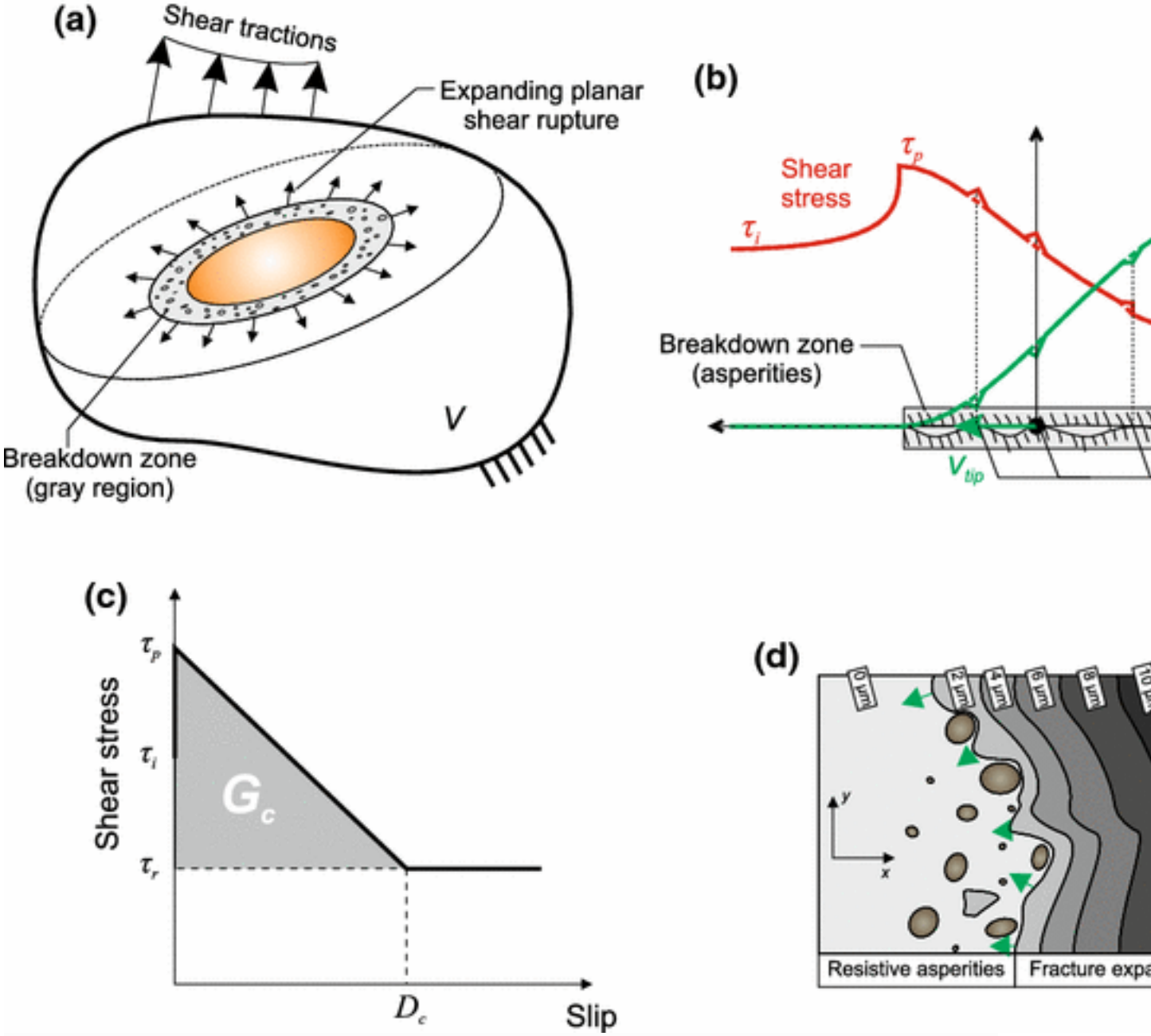

Fig. 1
a Schematic depiction of an expanding shear rupture along a frictional discontinuity within an elastic medium (*V*). The medium is subjected to shear tractions causing the shear rupture to expand. Stability of the rupture depends on its size and local stress states. At the fringe of the shear rupture is a breakdown zone. **b** Schematic diagram depicting the shear stress breakdown associated with slippage across the cohesive zone (gray region) of the crack tip. **c** The constitutive slip-weakening relation describing the relationship between shear stress drop and slip, where the (surface) fracture energy GcGc(units J m−2−2) is the area under the curve. **d** A cartoon

depiction of a resistive patch of asperities at the edge of the expanding shear rupture

3 Experimental Motivation

The modeling performed in this paper is aimed at developing an understanding of laboratory experiments performed between two bodies of polymethyl methacrylate (PMMA) in a direct shear configuration (Selvadurai 2015; Selvadurai and Glaser 2015a, 2017) and gain insight into its cohesive zone behavior. Selvadurai and Glaser (2017) reported on properties of individual asperity contacts measured experimentally using a pressure sensitive film. The pressure film (FUJI Prescale medium range 12–50 MPa) was compressed between the two PMMA bodies and was able to map the initial size, normal stress and locations of individual asperities. Results from the pressure sensitive film, which had been compressed at $\sigma_n \sim \sigma n \sim$ 0.8 MPa, are shown in Fig. 2a—adapted from Selvadurai and Glaser (2015a). Asperities are represented using a circular representation (with sizes proportional to the legend) when in actuality their shapes are more convoluted. Spatial histograms (black bars) showing the number of asperities along the *x*- and *y*-directions are shown on a 125 by 25 sized grid. From the results, we see that the distribution of asperities is non-uniform over the entire fault. These irregularities represent concentrations in normal stress and are indicative of strength barriers that resisted relative motion, i.e., slip, along the fault. A substantial concentration of asperities was recorded between $x \sim x \sim$ 150 to 300 mm, and they resisted the propagation of slow premonitory slip (Fig. 5 in Selvadurai and Glaser 2015a). This region was also responsible for the generation of precursory acoustic emission (AEs) during the nucleation phase. Selvadurai and Glaser (2015a) reported 68 AEs produced by the localized, dynamic failure of individual highly stressed asperities all recorded using an array of piezoelectric sensors (PZT) from the highly heterogeneous region. Each localized asperity failure radiated seismic energy in the form of elastodynamic stress waves, indicating that failure on the localized region propagated at a speed close to the shear wave velocity of the material. These stress waves had clear P and S wave phases which allowed for the location of the events—found to emanate from the seismogenic region (red region in Fig. 2a). An example of an AE captured by the PZT array is shown in Fig. 2b. Selvadurai et al. (2017) investigated the source physics (Brune 1970; Udías et al. 2014) associated with the radiated seismic energy and found them to be physically similar to earthquakes at larger scales. They found source mechanics, i.e., source radii *a* (m) and seismic moments $M_0 M0$ (Nm) (Kanamori and Heaton 2000; Abercrombie and Rice 2005), scaled from laboratory scale ($\sim\sim$ millimetric) to field scales ($\sim\sim$ kms). Recent studies are confirming these observations in various laboratory scenarios. The scaled seismicity is occurring on frictional interfaces, independent of the material (rocks and glassy polymers) and in different loading configurations [direct shear (Selvadurai

and Glaser 2015a), biaxial (McLaskey et al. 2014) and triaxial (Yoshimitsu et al. 2014)]. This is an indication that the presence of these events is in fact an intrinsic feature associated with stress breakdown during the nucleation of a frictional shear rupture.

Open image in new window

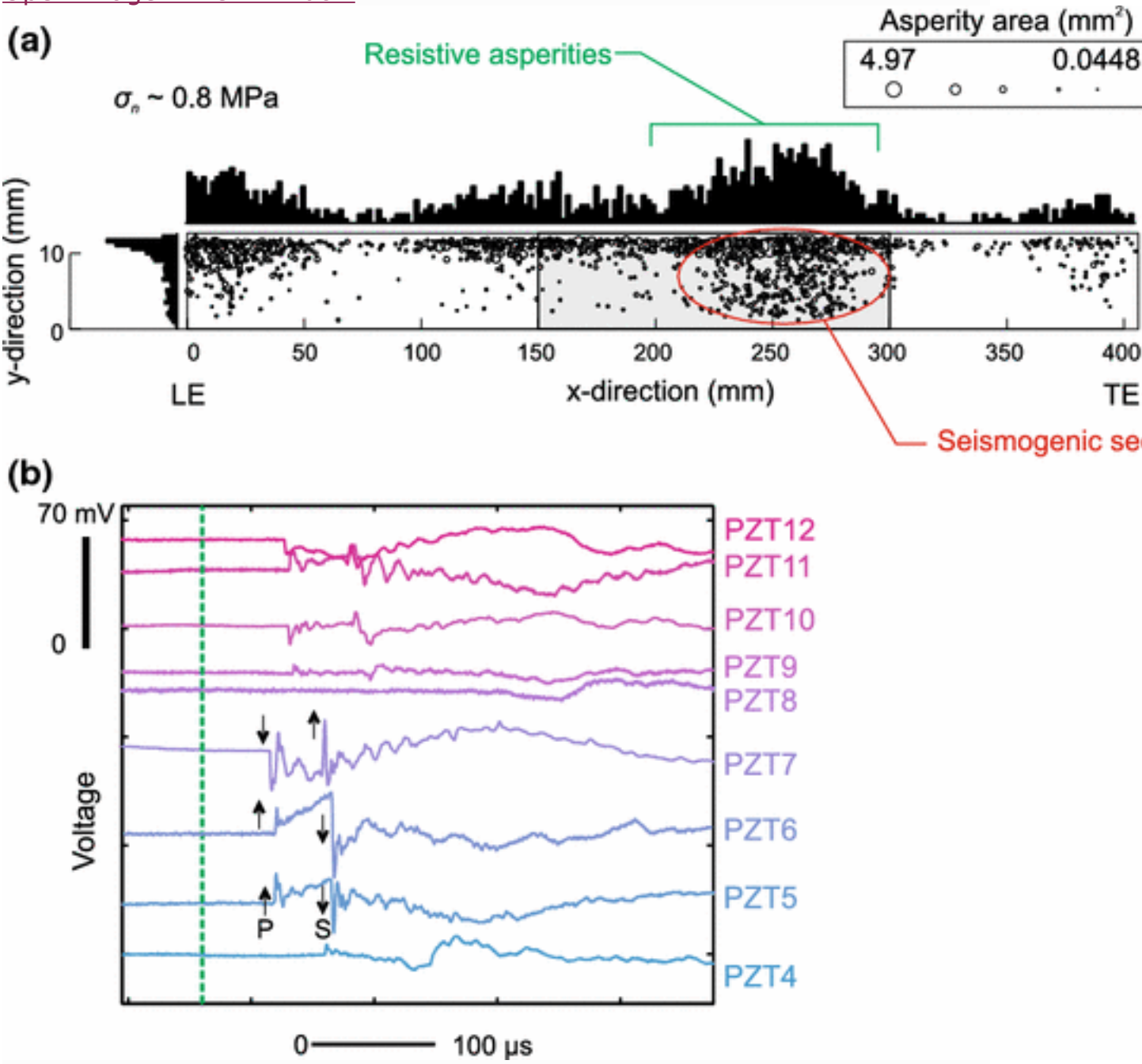

Fig. 2

Adapted from Selvadurai (2015). **a** Measurements of the non-uniform asperity distribution taken using the pressure sensitive film at the highest confining normal load. Spatial histograms of the asperity distribution are shown along the xx- and yy-axes for visual purposes (black bars). The

resistive patch of asperities was coincident with the location of acoustic emissions (AEs) that were recorded using a piezoelectric sensor array. **b** An example of an AE foreshock (FS), measured using the array of piezoelectric acoustic emission sensors (PZT4-PZT12), which were precursory to the impending main shock (i.e., gross fault rupture)

4 Modeling Asperities on an Idealized Planar Fault

We aim to develop a finite element (FE) model that helps build an understanding of the stress states, and the manner in which asperities communicate, which promote conditions favorable for the AEs associated with the localized failure of the highly stressed asperities. We choose to model the asperities so that they mimic the mechanical behavior of the so-called partial slip Cattaneo (1938) asperity (Mindlin 1949; Boitnott et al. 1992; Ciavarella 1998a, b; Yoshioka 1997; Dini and Hills 2009; Paggi et al. 2014). This model has been well investigated for engineering applications that involve load transfer by dry (unlubricated) friction in real engineering applications that are subjected to oscillatory loading (e.g., bolted joints, spline connections). Attempts to model fretting and fatigue failure of these joints (Nowell et al. 2006) are typical applications of the models. As discussed by Saltiel et al. (2017), the vibrational response of faults in nature can have implications on, for example, the low-frequency attenuation (or damping) (Saltiel et al. 2017) and constitutive behavior of the interface. Furthermore, frictional modeling that investigates dissipative effects of slip may help understand newer geophysical observations, such as, low-frequency earthquakes (LFEs), very low-frequency earthquakes (VLFs) and non-volcanic tremors (NVTs), which in certain cases have been attributed to oscillatory forcings and are constrained to the frictional fault (Peng et al. 2009; Houston et al. 2011).

5 Numerical Modeling of a Single Partial Slip Asperity

Cattaneo (1938) developed a solution (independently confirmed by Mindlin 1949) for an asperity contact patch formed between two elastic spheres under normal and tangential loading by applying friction at a smaller length scale to relate their shear tractions to normal pressures. This formulation was for smooth contact patches, but surface roughness has long been recognized to play a role (Greenwood and Williamson 1966). It is therefore beneficial to study multiple encounters (numerous asperities) in which their individual mechanical behavior obeys the original solution for the smooth contact. We first simulate a single, smooth contact using a finite element code ABAQUS (ABAQUS 2003). For details involved with the calibration of a single asperity contact, the reader is urged to consult Sects. 5.1 to 5.4 in Selvadurai and Glaser (2015a, b).

Figure 3a shows a schematic representation of a spherical elastic body (with a radius of curvature R) pressed against a rigid flat surface (Paggi et al. 2014). In our model, we would like to mimic its mechanical response using the numerical finite elements (FE). The gray line shows the exaggerated deformations under only normal forces P, and the black dashed line shows the exaggerated deformations with the addition of tangential load Q. As the tangential load is increased, slip accrues along the periphery of the contact region while the central portion remains stuck. Mindlin (1949) refers to this as incipient sliding. Johnson (Ch. 7 in Johnson 1985) has presented the full derivation for the partial sliding spherical asperity against a flat plate. The relationship between the non-dimensional slipping region (c_0/a_0c0/a0) to non-dimensional shearing force ($Q/\mu*P$Q/μ∗P) is given as

$$c_0a_0=(1-Q\mu*P)^{1/3},c0a0=(1-Q\mu*P)1/3, \quad (1)$$

where $\mu*$μ∗ is the coefficient of friction, a_0a0 is the initial size of the contact radius, c_0c0 is the size of the 'stuck' radius, and P and Q are, respectively, the normal and shearing forces calculated by integrating the appropriate stresses over the contact surface ($0 <r\leq a_0$<r≤a0). Ciavarella (1998a, b) generalized the Cattaneo partial slip problem for single, multiple and periodic contacts and, more recently, Paggi et al. (2014) formulated the problem for statistically rough surfaces. Selvadurai and Glaser (2015a) used an FE model to capture a similar response to the partial slip asperity described in Eq. (1) that we build upon here.

Our numerical model uses a classic Hookean isotropic elastic slider (Davis and Selvadurai 1996) that was sheared across a rigid base plate. The ABAQUS code adopted a finite sliding computational algorithm to compute the slip displacements occurring along the interface. The relationship between the contact shear stress and relative shear deformation was

$$\tau=k_s\delta for \tau<\mu*\sigma*,\tau=ks\delta for\tau<\mu*\sigma*, \quad (2)$$

where $\sigma*$σ∗ is the normal stress on the individual element and the shear stiffness $k_s=\mu*\sigma*/\gamma_{crit}$ks=μ∗σ∗/γcrit. The local coefficient of friction $\mu*$μ∗ (0.5 for all simulations reported here) and the maximum elastic slip distance γ_{crit}γcrit were specified to be a function of the characteristic length of the element (length scale). In our study, maximum elastic slip distance (γ_{crit}γcrit) was set to 0.005 times the element characteristic dimension, i.e., length scale of an element (ABAQUS 2003). Non-contact elements were given a coefficient of friction $\mu*=0$μ∗= 0. The response of the ABAQUS model versus Eq. (1) is presented in Fig. 3b. The inset images in Fig. 3b show the sticking elements (red) and sliding elements (green) as the non-dimensional shearing force ($Q/\mu*P$Q/μ∗P) was increased.

Open image in new window

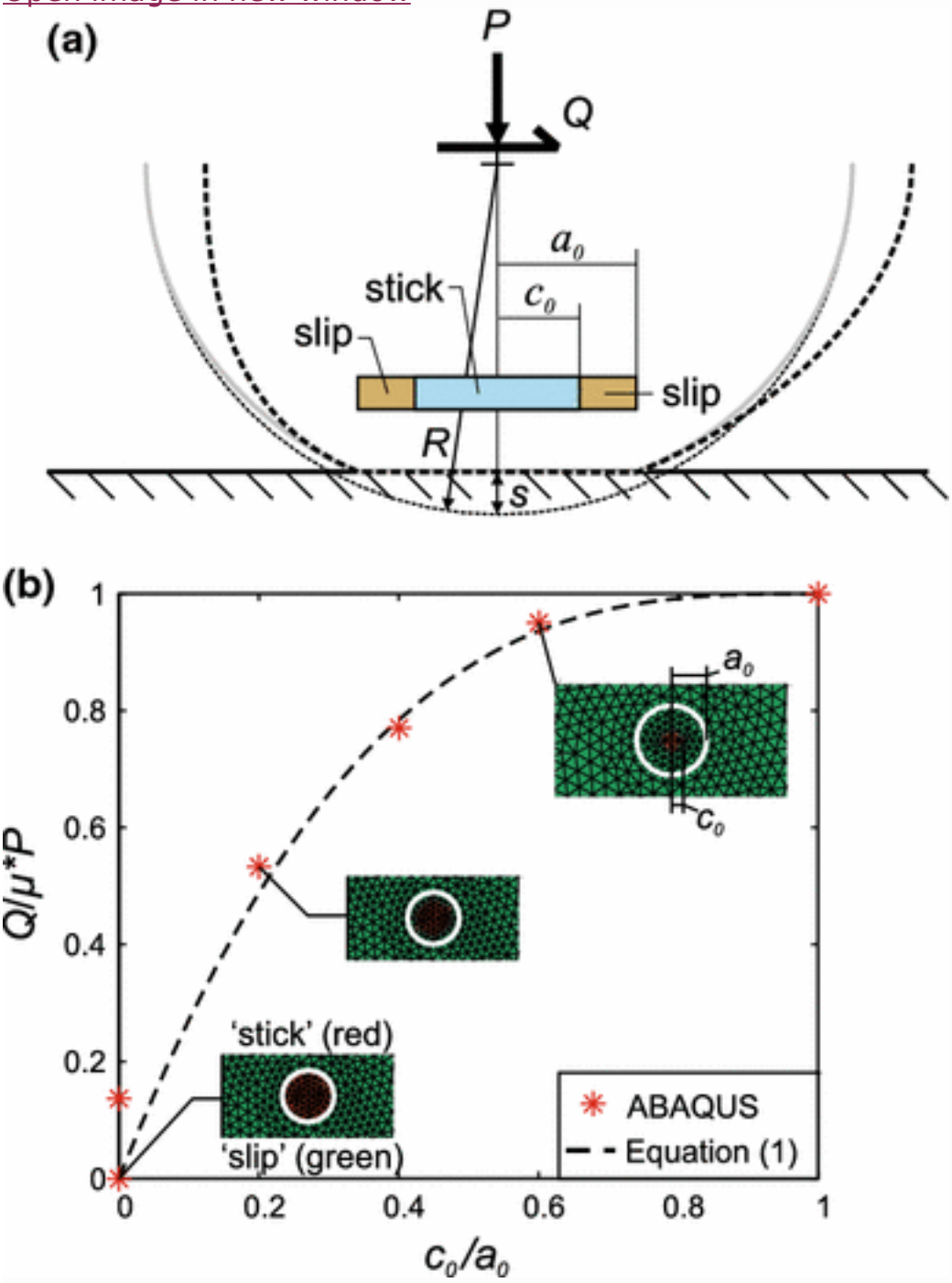

Fig. 3
a Schematic drawing of a single asperity compressed and then loaded tangentially (adapted from Paggi et al. 2014). Due to loading, slip accrues along the periphery of the contact area and grows inward with increasing shearing. **b** Results from calibration model (see Selvadurai and Glaser 2015a). ABAQUS results for the non-dimensional slipping region

(c_0/a_0c0/a0) versus the non-dimensional shear force ($Q/\mu*P$Q/μ∗P) are presented against Eq. (1)

6 Numerical Modeling of the Experimental Multiple Asperity Interface

There have been efforts made to understand frictional behavior of multi-contact interfaces in the context of the partial-asperity (Ciavarella 1998a, b; Dini and Hills 2009; Medina et al. 2013; Li et al. 2011; Paggi et al. 2014). Most studies that investigate frictional mechanics in this manner assume an idealized rough half-space and assume isometric asperity distributions (Dini and Hills 2009; Medina et al. 2013; Li et al. 2011). In our study, we use finite elements (FE) to understand the bulk frictional behavior of the experimentally measured non-uniform distributions of asperities. We will also provide a brief numerical study into how the statistical size distribution of asperities can affect the frictional behavior from synthetically generated surfaces (see Sect. 7.2).

Figure 4a shows the computational mesh used for the multiple asperity model of the experimental interface. It was composed of 1,068,845 linear tetrahedral elements (C3D4). As in the calibration model, the interface was not allowed to separate from the rigid base (not shown). Shear stress along the fault was increased by incrementally increasing the far-field displacement ($u_x=\Delta_{step}$ux=Δstep) shown by black arrows on the top of the elastic slider shown in Fig. 4b. The Young's modulus $E=6180$E=6180 MPa and Poisson's ratio $\nu=0.32$ν=0.32 were prescribed to the model, and incremental strains were computed using

$$d\epsilon_{ij}=\frac{d\sigma_{ij}}{2G}-\frac{\lambda*\cdot d\sigma_{kk}\delta_{ij}}{2G(3\lambda*+2G)} \quad (3)$$

where $\lambda*$λ∗ is the Lamé's first parameter, *G* is the shear modulus (2341 MPa), and summation over the repeated indices is implied. Pressure sensitive film measurements of the initial contact distribution between $x=182.5$x=182.5 to 257.5 mm were used to define the locations and sizes of the asperities in the computational model (see Fig. 2a). The interface shown in Fig. 4b is composed of 172 circular asperities (red) surrounded by the frictionless interface (green). Due to computational restrictions, only larger asperities with areas exceeding 0.125 mm^2mm2 were modeled and only a small section of the interface along the *x*-direction (dimensions $L=75$L=75 mm ×× $W=12.7$W=12.7 mm) was numerically modeled. The off-fault dimension of the elastic slider was $B=100$B=100 mm in the *z*-direction. We performed simulations for a range of prescribed asperity normal stress ($\sigma*=50$σ∗=50, 70, 90 MPa) in

which each of the 172 asperities were prescribed a uniform pressure boundary condition. Elements were forced into slipping states by increasing the far-field displacement $\Delta_{step}\Delta step$ at 1 μμm increments. We employ a quasi-static solver, and no inertial effects are treated in these calculations—dynamic failure (i.e., production of seismic waves) is not modeled. This study is focused on understanding the quasi-static changes in stress states along the interface and how they evolve in the context of contact mechanics and the partial slip asperity.

Open image in new window

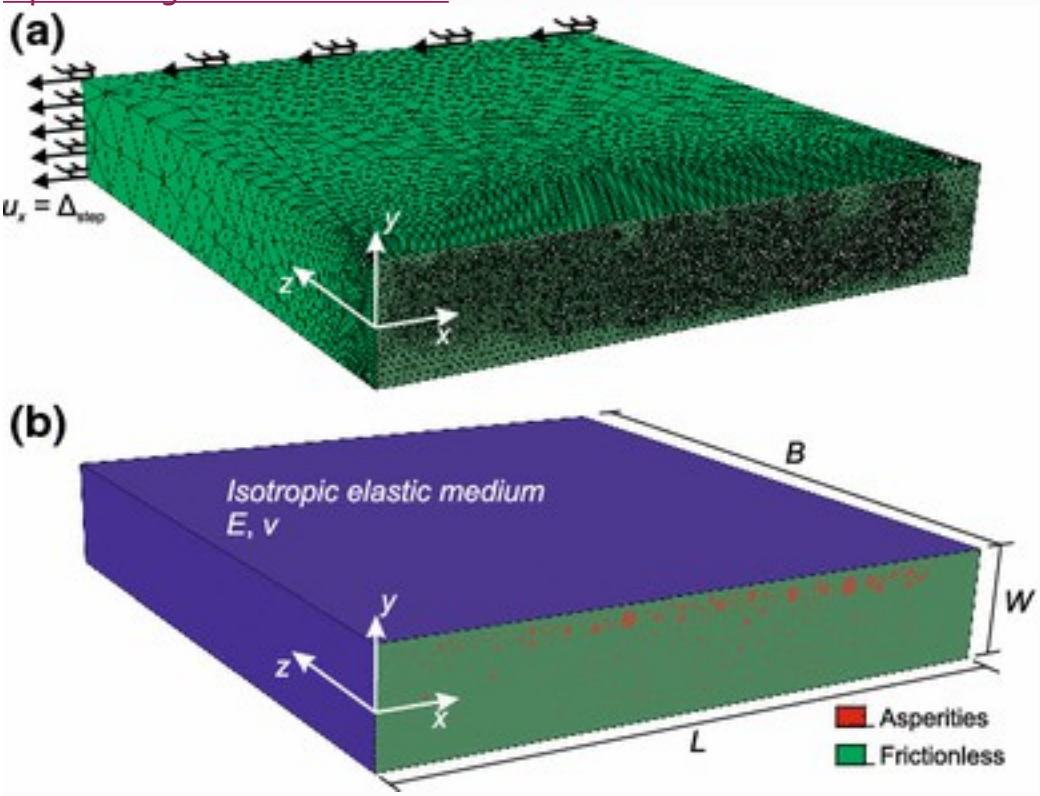

Fig. 4

a The computational mesh used to model the frictional behavior from the experimentally measured asperity locations. **b** The frictional interface (W×LW×L) with asperity sizes and locations taken from the pressure sensitive film. Asperities (red) obeyed the finite friction formulation (Eq. (2) with $\mu*=0.5\mu*=0.5$), whereas green elements were assumed to be frictionless $\mu*=0\mu*=0$. (NB The discoloration of the image near regions of high mesh refinement is due to image rendering issues) (color figure online)

6.1 Mesh Refinement and Solution Convergence

Due to the lack of a theoretical solution for the multi-asperity model shown in Fig. 4b, we tested the model's convergence and performed a mesh sensitivity analysis. We considered convergence as the steady-state value of average shear stress along the interface as all contacts were forced into the sliding regime. When all asperities have entered the sliding regime, the

deformation gradient throughout the model is zero (Timoshenko and Goodier 1970) and the model is considered to be at steady state (see Sect. 5.6.1 in Selvadurai and Glaser 2015a). The mesh sensitivity analysis was performed on the synthetic distribution of equally sized asperities shown in Fig. 5a. The total real contact area $A_r=84.33mm^2$ with each asperity having an area $A_i=0.5mm^2$ leaving $N=168$ asperities along the interface. Asperities were randomly distributed in space, defined by the random search algorithm in MATLAB (MATLAB 2014). Asperities were not allowed to be spaced within 2.1 radii of each other.

The nonlinear constitutive relationship between average shear stress $\bar{\tau}$ to average slip $\bar{\delta}$ is shown in Fig. 5b for different levels of mesh refinement. The average slip $\bar{\delta}$ was calculated as the magnitude of slip between the *x*- and *y*-directions (i.e., $\bar{\delta}^2=\bar{\delta_x}^2+\bar{\delta_y}^2$) averaged for every integration point along the interface. Again, we assumed that there is no fault dilatation ($\delta_z=0$). The average shear stress $\bar{\tau}$ was calculated as the magnitude of shear tractions between the *zx*- and *yz*-directions (i.e., $\bar{\tau}^2=\bar{\tau}^2_{zx}+\bar{\tau}^2_{xy}$) averaged over every numerical integration point along the interface. As the amount of tetrahedral elements were increased, the steady-state value of average shear stress converged to $\bar{\tau}\sim$ 3.41 MPa. Increasing the number of elements from 441,080 (cyan line) to 1,122,984 (dashed black line) resulted in less than 1% change in the steady-state value of $\bar{\tau}$. As seen in Fig. 4a, the majority of the mesh refinement was performed at the interface and in the first 5 mm in the *z*-direction. All asperities were discretized with a minimum of 20 elements about its periphery in all simulations reported here.

Open image in new window

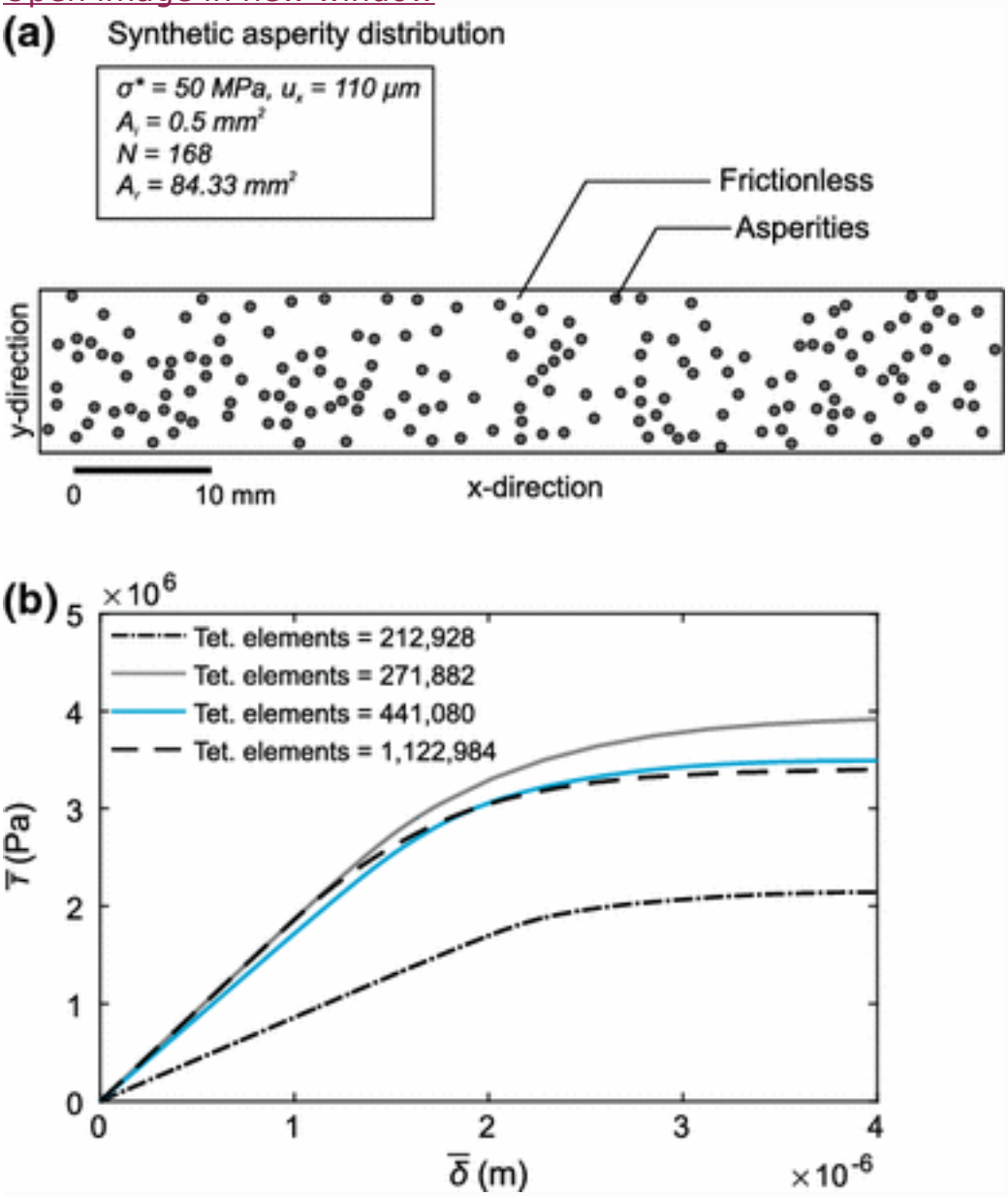

Fig. 5
a Synthetic distribution of equally sized asperities used for the mesh sensitivity analysis. **b** Traction-slip behavior for the synthetic asperity distribution in (**a**) with an increasing number of elements

7 Results

7.1 Bulk Traction-Slip Behavior of the Experimental Interface

We show the hysteretic response of the experimentally constructed interface under a cyclical far-field loading condition. Until recently cyclical loading was not something considered to affect faults in nature. Studies examining this cyclical phenomenon were typically frictional processes in engineering-

related activities (e.g., clutches, brakes, bearings) where fretting or fatigue failure was needed to be characterize the system in a simplistic model. Omitting oscillatory loading on faults may be an oversimplification in view of recently observed nonstandard earthquake signals (LFEs, VLFs, NVTs, among others), which are believed to be triggered by low-stress vibrational (oscillatory) forcings. In this section, we show the hysteretic response of the experimental interface (Fig. 4b) under cyclical far-field loading conditions. While the complex dynamics occurring due to high-frequency excitation (Kostić et al. 2014) are not captured here, our simulations have the ability to quantify the low-frequency dissipative energy released, an important feature when quantifying frictional heating—a large portion of the energy released during an earthquake (Scholz 2002).

To examine the hysteretic response of the experimental interface, the far-field displacement boundary conditions $u_x$ux were varied in a stepwise manner and the resulting traction-slip behavior was calculated. An individual cycle was divided into three regimes: (1) initial loading, where $u_x$ux was incrementally increased to a certain value, (2) unloading, where $u_x$ux was incrementally decreased to the negative value of the initial loading regime, and (3) reloading, where $u_x$ux was incrementally increased to the same value as the initial loading regime. The blue line in Fig. 6a shows an example of the numerically calculated traction-slip behavior for asperities with normal stresses of $\sigma*=50\sigma*=50$ MPa and where the far-field loading surface was incrementally moved to the position $u_x=75\mu ux=75\mu$m ($+5\mu+5\mu$m increments == 15 steps), then unloaded to the position $u_x=-75\mu ux=-75\mu$m ($-5\mu-5\mu$m increments == 30 steps) and re-loaded to $u_x=75\mu ux=75\mu$m ($+5\mu+5\mu$m increments = 30 steps). Figure 6a also shows the hysteretic behavior for asperities exhibiting an identical level normal stress ($\sigma*=50\sigma*=50$ MPa) but with varying levels of far-field displacements: $u_x=\pm ux=\pm$ 55 μμm (black line), $u_x=\pm ux=\pm$ 75 μμm (blue line) and $u_x=\pm ux=\pm$ 110 μμm (red). Convergence of the numerical solution was achieved by taking steps of 15–30–30 to solve the load-unload-reload regimes, respectively, regardless of the magnitude of $u_x$ux. For the case where cycling occurs between $u_x=\pm ux=\pm$ 110 μμm (red line), the slope of shear stress with respect to sliding becomes zero (i.e., $d\bar{\tau}/d\bar{\delta}=0d\bar{\tau}/d\bar{\delta}=0$) before the end of the first loading cycle. This is indicative of ‘full sliding’ conditions over the entire fault, i.e., all asperities along the interface had entered sliding and the deformation gradient in the model was zero. As the fault was unloaded, residual slip affected the traction-slip response, which followed a hysteresis loop. The area bounded by the hysteresis loop *D* (gray regions in Fig. 6a, b) represents the dissipative/frictional energy expenditure and is shown in both panels of Fig. 6 for the case where $\sigma*=50\sigma*=50$ MPa

and $u_x = \pm ux = \pm$ 75 μμm. While not explicitly calculated, larger values of *D* are apparent when more frictional sliding occurs along the interface and is indicative of a higher amount of frictional energy released. For the case with lower levels of far-field loading $u_x = \pm ux = \pm 75$ μμm (blue line) and $u_x = \pm ux = \pm$ 55 μμm (black line), the fault was not driven to its full sliding state ($d\bar{\tau}/d\bar{\delta} \neq d\bar{\tau}/d\bar{\delta} \neq 0$), indicating that some elements on the asperities remained in the 'stuck' regime, which resulted in less frictional sliding and lower amounts of frictional dissipation *D*.

We quantified the frictional dissipation *D* graphically using the area calculator in the vector graphics editor CorelDraw X7 (Bouton 2014). The algorithm converted the curves to a polygon using an Euler method and estimated the area in units $mm^2 2$. This was then converted to units of J $m^{-2} - 2$ from a proportional square made about the original axes limits within the vector graphics editor (i.e., 640 J $m^{-2} = 2164 mm^2 - 2 = 2164 mm2$). We found the frictional dissipation for $u_x = \pm ux = \pm 55$ μμm was $D = 4.4 D = 4.4$ J $m^{-2} - 2$ (black line), $u_x = \pm ux = \pm$ 75 was μμm $D = D =$ 76 J $m^{-2} - 2$ (blue line) and $u_x = \pm ux = \pm 110$ μμm was $D = D =$ 544 J $m^{-2} - 2$(red). We see that the fault dissipates more energy when the magnitude of $u_x ux$ is higher for the same normal stress. For this specific distribution of asperities, when $u_x ux$ was increased from ± 55 to ± 75 μμm (36% increase) we saw a ∼∼ 1630% increase in *D*and when $u_x ux$ was increased from ± 75 to ± 110 μμm (47% increase) we saw a ∼∼ 615% increase in *D*. These disproportional changes are representative of the highly nonlinear behavior of the traction-slip behavior and its dependence on the normal stress and whether the interface has entered the 'full sliding' regime.

Figure 6b examines the effect of normal stress on the traction-slip response. Response for three levels of asperity normal stress $\sigma* = 90 \sigma* = 90$ MPa (black line), $\sigma* = 70 \sigma* = 70$ MPa (red line) and $\sigma* = 50 \sigma* = 50$ MPa (blue line) is shown for the same amount of far-field loading $u_x = \pm ux = \pm$ 75 μμm. We saw that at lower levels of normal stress, more elements along the interface were driven to sliding resulting in higher levels of frictional dissipation *D* than at higher loads. At higher loads, the interface also behaved in a more stiff manner during the initial portion of the loading regime. The same technique was used to calculate the frictional dissipation as before. We found the frictional dissipation for asperity normal stress $\sigma* = 90 \sigma* = 90$ MPa was $D = 21 D = 21$ J $m^{-2} - 2$ (black line), $\sigma* = 70 \sigma* = 70$ MPa was $D = 40 D = 40$ J $m^{-2} - 2$ (red line) and $\sigma* = 50 \sigma* = 50$ MPa was $D = 76 D = 76$ J $m^{-2} - 2$(blue line). We see that the fault dissipates more energy through friction when loaded with lower normal stress. For this specific distribution of asperities, when $\sigma* \sigma*$ was increased from 50 to 70 MPa (40% increase) we saw a 47% decrease

in D and when $\sigma*\sigma*$ was increased from 70 to 90 MPa (29% increase) we saw a 47.5% decrease in D.

Open image in new window

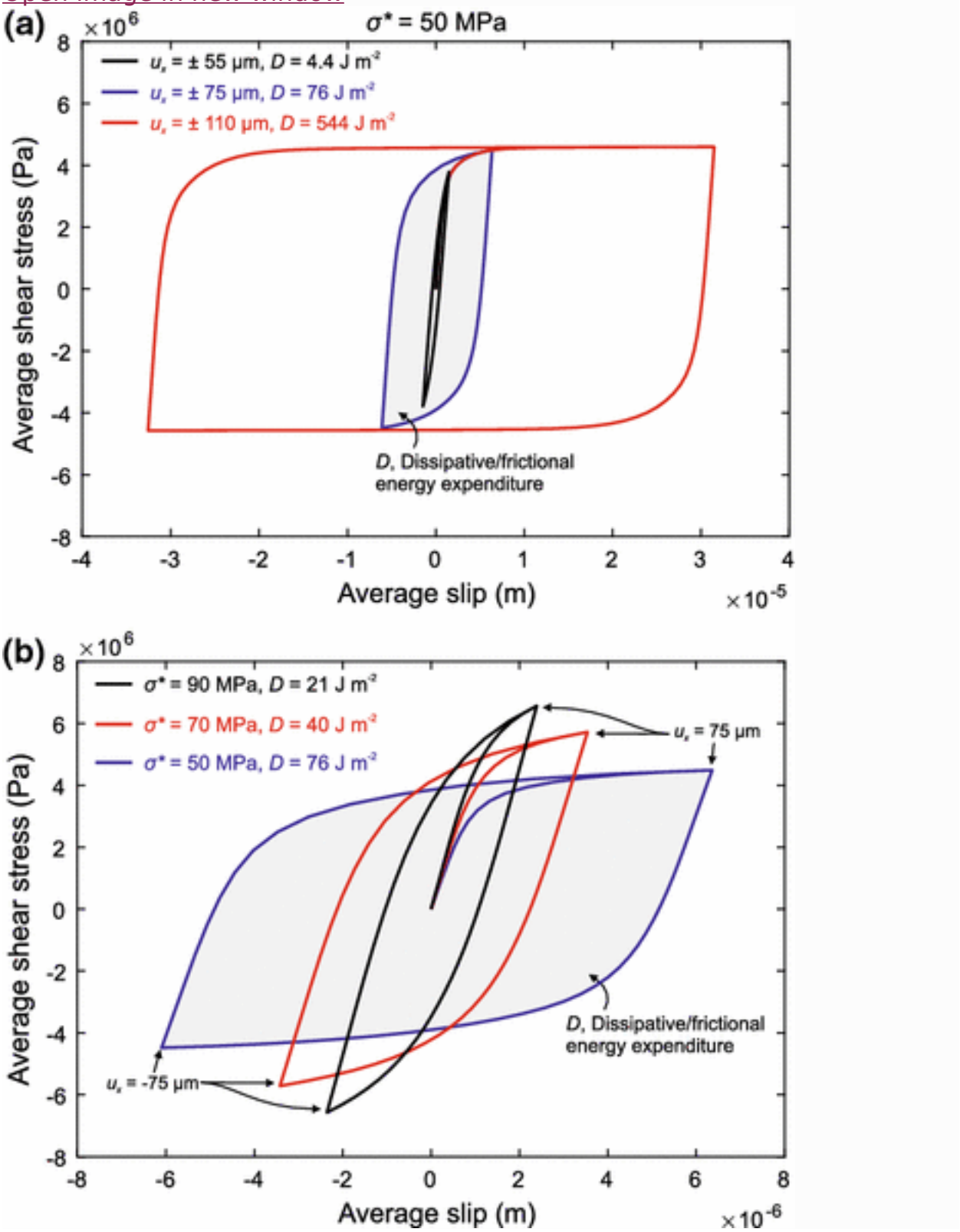

Fig. 6
a Nonlinear traction-slip relationship for the fault confined to the same normal stress ($\sigma*=50\sigma*=50$ MPa) but cyclically loaded to $u_x=\pm ux=\pm$ 110 μμm (red line), ± 75 μμm (blue line) and ± 55 μμm (black line). **b** Variation in the traction-slip behavior for asperity normal stresses of $\sigma*\sigma*$ = 50 MPa (blue line), $\sigma*\sigma*$ = 70 MPa (red line) and $\sigma*=90\sigma*=90$ MPa (black line) for identical levels of loading ($u_x=\pm ux=\pm$ 75 μμm) (color figure online)

7.2 Bulk Traction-Slip Behavior of Synthetic, Lognormal Size Distributions of Asperities

In this section, we control the random distribution of asperities along the interface in a similar manner to that described in Sect. 6.1. The goal here is to provide some insight into the behavior of experimental model (Fig. 6) but for lognormal size distributions of asperities with random spatial distributions—a feature that has been observed in previous laboratory experiments (Yoshioka and Scholz 1989; Yoshioka and Iwasa 1996; Yoshioka 1997; Wang and Scholz 1995).

In Fig. 7a, we present a set of three synthetic interfaces each expressing a lognormal distribution of asperity sizes. The log-mean and log-standard deviations were determined for the lognormal fit to the experimental asperity sizes and used as the basis for each distribution in Fig. 7a. For each synthetic case, we conserved the real contact area (A_rAr = 84.33 $mm_2 2$) from the experimentally determined numerical model in Fig. 4b. The mean asperity area was held constant ($A_i \sim Ai\sim$ 0.5 $mm_2 2$) while we varied the width of the lognormal distribution (Fig. 7b). The widths of the synthetic distributions were stretched by multiplying the experimental log-standard deviation by 0.2 (top panel, **case 1**, red), 0.5 (middle panel, **case 2**, blue) and 0.8 (bottom panel, **case 3**, green). The probability distribution functions (Fig. 7b) clearly show that the lognormal distributions of asperities sizes broaden from case 1 to 3. Traction-slip behaviors were computed for each case and are shown in Fig. 7c. The colors are indicative of the associated distributions in Fig. 7b. For these computations, the asperity normal stress was prescribed to be $\sigma*\sigma*$ = 50 MPa and the far-field displacements were incrementally increased to $u_x ux$ = 75 μμm. We have incorporated the results from Fig. 5b for the end-member case 4, where asperity sizes were constant ($A_i Ai$ = 0.5 $mm_2 2$).
Frictional dissipation D was calculated using the graphical techniques for the loading curves shown in Fig. 7c. The dissipation was taken as the area under the traction-slip response, where the fault was loaded then unloaded to $\tau^-\tau^-$ = 0. We found for: case 1 D = 7.75 J $m_{-2} -2$, case 2 D = 8.64 J

m−2−2, case 3 D = 11.1 J m−2−2, the end-case member case 4 (uniform sizes) D = 19.5 J m−2−2and the experimental interface D = 17.5 J m−2−2. Comparing the synthetic interfaces, we see that most frictional dissipation (D) was observed on the interface with the broadest distribution of asperities (green line, case 3) for these specific loading conditions and excluding case 4 (uniform distributions). This interface was also the most compliant $\bar{\tau}/\bar{\delta}=1.321\times10^{12}\bar{\tau}/\bar{\delta}=1.321\times1012$ Pa m−1−1. For the tightest lognormal distribution (red line, case 1), we observed the lowest amount of frictional dissipation and noted that the interface was initially more stiff than cases 2 and 3. The uniform size distribution, case 4, was the most stiff $\bar{\tau}/\bar{\delta}\sim1.86\times10^{12}\bar{\tau}/\bar{\delta}\sim1.86\times1012$ Pa m−1−1 and had the most frictional dissipation. At the end of the loading cycle, i.e., $u_x u_x$ = 75 μμm, the average shear stress accommodated by case 1, case 2 and case 3 was $\bar{\tau}\sim\bar{\tau}\sim$ 3.24, 3.10 and 2.94 MPa, respectively, and average slip was $\bar{\delta}=4.46\bar{\delta}=4.46$, 5.06 and 6.24 μμm, respectively. For the end-member case 4, we see that the interface accommodated higher amounts of average shear stress $\bar{\tau}\sim\bar{\tau}\sim$ 3.41 MPa and slip $\bar{\delta}\bar{\delta}$ = 7.68 μμm for the same loading conditions as the surfaces with variable sizes of asperities. However, end-member case 4 had entered full sliding conditions (indicated by the vertical arrow in Fig. 7c), leading to the most frictional dissipation of all the interfaces for these loading conditions. All synthetic surfaces (cases 1 through 4) showed similar traction-slip behaviors with slight variations owing to the respective broadness of their lognormal size distributions. In Fig. 7c, we have also superimposed the experimental model (thick gray line) for the same loading conditions. Visually we see that the response is quite different from the synthetics. The experimental fault displays high shear stiffness $\bar{\tau}/\bar{\delta}\sim3.19\times10^{12}\bar{\tau}/\bar{\delta}\sim3.19\times1012$ Pa m−1−1 then softens considerably after accruing $\bar{\delta}\sim\bar{\delta}\sim$ 1.6 μμm of slip. Wang and Scholz (1995) noted a similar behavior on frictional experiments (Wang and Scholz 1994) and attributed it to various mechanisms contributing to the surface energy (initial friction, asperity interlocking, surface evolution). We, however, can explain this behavior from the irregular spatial distribution of asperities seen in Fig. 4b and an understanding of how shear stiffness is affected by the number an average radii of asperities on the interface. From our simulations, we see that, initially, the fault consists of many localized patches of small asperities. This lends to the initially high shear stiffness and can be seen by comparing case 1 and case 3. The simple increase in small asperities present in case 1 leads to high shear stiffness, which will be confirmed in the next section with our discussion on interfacial shear stiffness derived from the mechanical solution of interacting spherical asperities (Mindlin 1949; Berthoude and Baumberger 1998). Once the shear stress has increased passed a certain value, the fault begins to behave more compliantly. This may be explained assuming that as shear stress increased the smaller asperities were driven (more easily) to the full sliding conditions

since, spatially, they are not ‘shielded’ by the larger asperities. We can see in Fig. 4b that the larger asperities are asymmetrically distributed to the upper section of the fault, where the upper section is defines as $y>0$. Conversely, the lower section $y<0$ had a population of predominantly smaller asperities. Once the smaller/non-shielded asperities become ‘unstuck’, the fault behaved more like the case 3 since the large asperities dominate the traction-slip behavior, lending to the more compliant behavior in our computations.

Open image in new window

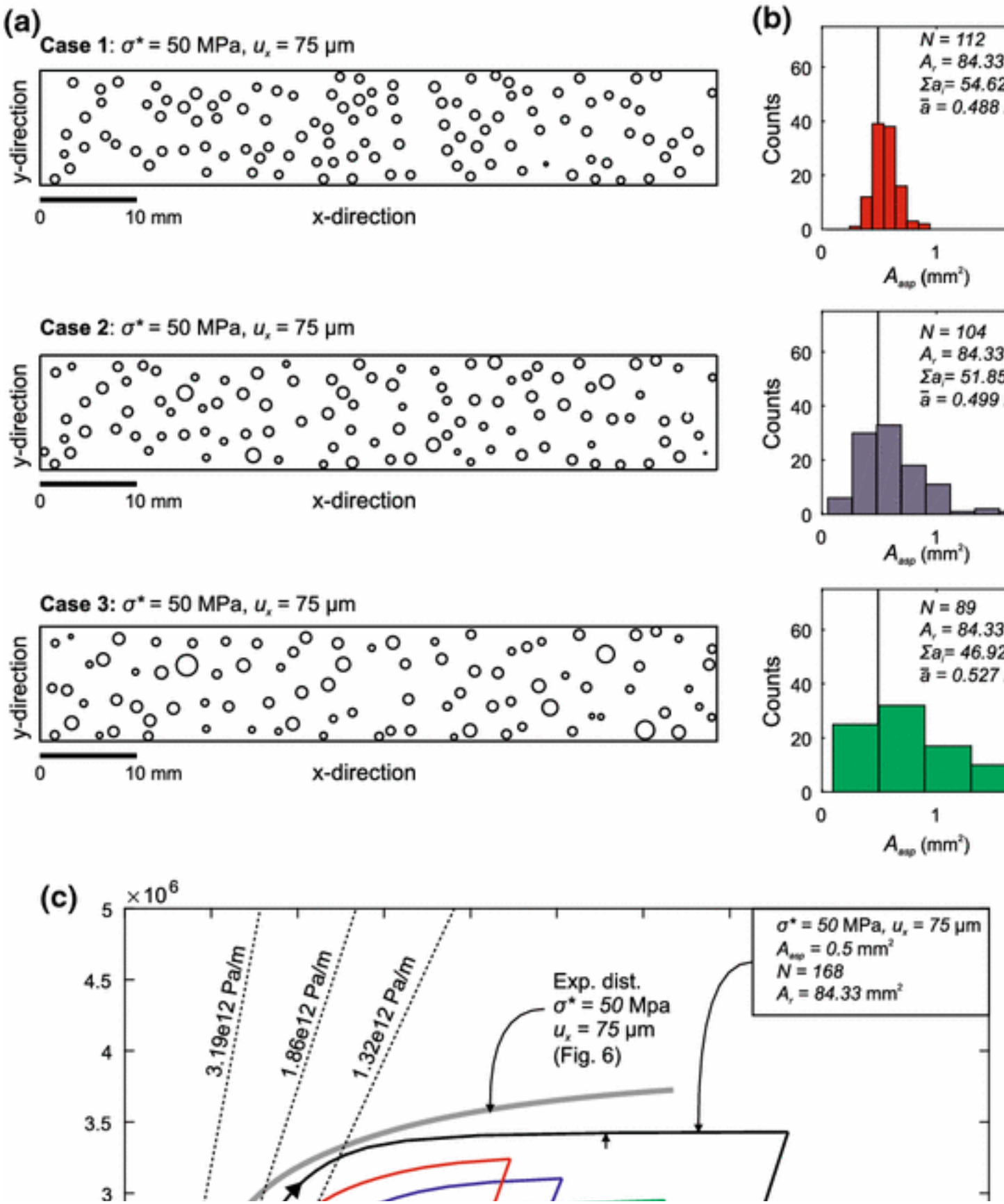
(a)
Case 1: σ* = 50 MPa, u_x = 75 μm
y-direction
0
10 mm
x-direction
Case 2: σ* = 50 MPa, u_x = 75 μm
y-direction
0
10 mm
x-direction
Case 3: σ* = 50 MPa, u_x = 75 μm
y-direction
0
10 mm
x-direction
(b)
N = 112
A_r = 84.33
Σa_i = 54.62
ā = 0.488
Counts
A_asp (mm²)
N = 104
A_r = 84.33
Σa_i = 51.85
ā = 0.499
Counts
A_asp (mm²)
N = 89
A_r = 84.33
Σa_i = 46.92
ā = 0.527
Counts
A_asp (mm²)
(c)
×10^6
3.19e12 Pa/m
1.86e12 Pa/m
1.32e12 Pa/m
Exp. dist.
σ* = 50 Mpa
u_x = 75 μm
(Fig. 6)
σ* = 50 MPa, u_x = 75 μm
A_asp = 0.5 mm²
N = 168
A_r = 84.33 mm²

Fig. 7
a Synthetic distributions of asperities where the size distributions followed certain attributes of the experimental model. For each synthetic, the width of the lognormal size distribution varied from the top (**case 1**, tight) to the bottom (**case 3**, broad). **b**Probability distribution functions of the asperity distributions for **case 1** (top), **case 2**(middle) and **case 3** (bottom). **c** Traction-slip response for each case 1 to 3. The end-member case 4 is the uniform size distribution shown in Fig. 5a. The experimental traction-slip behavior (gray line), for similar loading conditions, is shown for comparison with the synthetic surfaces

7.3 Variation in Tangential Stiffness Due to Width of Lognormal Asperity Distribution

The tangential stiffness of the interface, shown in Fig. 7c for case 3, the widest asperity distribution, and case 4, the control set of uniform asperity sizes, is observed to decrease as the width of the distribution grows. This follows the predicted theoretical stiffness equation of Medina et al. (2013) (see also Berthoude and Baumberger 1998) where the tangential stiffness is observed to decrease systematically as the distribution of asperity radii grows wider.

To further investigate the applicability of the results from Medina et al. (2013), we take their equation for the tangential stiffness of a general interface, assuming the asperities are sufficiently widely spaced to be treated independently. Tangential stiffness is given by

$$\kappa_T = 4E(1+\nu)(2-\nu)\sum a_i, \kappa T = 4E(1+\nu)(2-\nu)\sum ai, \tag{4}$$

where E is the Young's modulus, $\nu\nu$ is the Poisson's ratio, and $a_i ai$ is the individual asperity radius. We adjust their tangential stiffness for comparison to the slopes in Fig. 7c by dividing by the apparent area $\bar{\tau}/\bar{\delta} = \kappa_T/A_a \bar{\tau}/\bar{\delta} = \kappa T/Aa$. The sum of the asperity radii is shown for each distribution in Fig. 7b, and again we see that the observed results match the theoretical prediction—the stiffness decreases as the sum of the asperity radii decreases, all else held constant. The PMMA in our model has Young's Modulus E = 6180 MPa and Poisson's ratio $\nu\nu$ = 0.32. For the random distribution of uniformly sized asperities, shown as the gray hysteresis loop in Fig. 7c, the (apparent area adjusted) theoretical tangential stiffness is $7.84\times10_{11} 7.84\times1011$ Pa $m^{-1}-1$. For comparison, the experimental tangential stiffness shown in the figure is $1.86\times10_{12} 1.86\times1012$ Pa $m^{-1}-1$, a factor of 2.4 times larger than the theoretical. The widest distribution has a theoretical stiffness of $5.49\times10_{11} 5.49\times1011$ Pa $m^{-1}-1$ and an experimental stiffness

of $1.32\times10_{12}1.32\times1012$ Pa $m_{-1}-1$, also a factor of 2.4 larger than expected.

Next we investigate the validity of the sufficiently widely spaced asperities assumption using the empirically derived correction factor for randomly spaced asperities from Medina et al. (2013), which is given as

$$\kappa T\kappa T\infty=\exp[-1.3(ArA0)0.35],\kappa T\kappa\infty T=\exp[-1.3(ArA0)0.35], \quad (5)$$

where $\kappa T\infty\kappa\infty T$ is the theoretical tangential stiffness for infinitely widely spaced asperities calculated by the previous equation. This results in a correction factor of 0.57 for the real contact area used in our simulations, further reducing the theoretical tangential stiffnesses so that the experimental stiffnesses are 4.1 times larger than theorized. Although the theoretical stiffnesses do not match our experimental results, we are encouraged by the relatively small factor of error and, more importantly, by the constant factor across multiple tests. Differences between the models used by Medina et al. (2013) and our models, such as size of the model and choice of boundary conditions, could plausibly account for a linear offset of this scale between our results and the theory.

8 Conclusions

We have built an more refined understanding of faulting behavior based on a FE model that incorporates variable distributions of partial slip asperities that introduce strength heterogeneity along a planar fault. This numerical study was motivated to better understand the initial conditions that may be contributing to the experimentally observed AEs produced along a laboratory fault as it was sheared to failure. Previous models, which do not incorporate strength heterogeneity, are unable to capture the faulting stress states that would promote the production of localized fault plane AEs. While our simulations are quasi-static and do not simulate the stress waves produced by the AEs (i.e., elastodynamics), they do build on our understanding of contact mechanics and investigate stress conditions and faulting behavior (i.e., traction-slip relationship) that may promote favorable conditions for the production of these AEs.

Traction-slip behavior throughout the fault load cycle was modeled using an experimentally measured asperity distribution. Asperities represented local strength heterogeneity that will ultimately affect the accumulation of premonitory slip during the nucleation cycle. Our finite element representation of strength heterogeneities (asperities) included the location and sizes of asperities that were taken directly from an experimental pressure sensitive film; the distribution was not chosen by the modeler. Each asperity obeyed the validated, single Cattaneo (1938) partial slip asperity. Building on this solution, we then constructed a multiple asperity interface using the experimental data from the pressure film. The model showed that

as bulk shear stress was increased along the fault, average slip was dependent on both the asperity distributions and magnitude of normal stress. By loading the fault in a cyclical manner, we were able to characterize the constitutive behavior and frictional dissipation during the fault's hysteretic response. This normal stress-dependent constitutive relationship may be helpful to both the fields of engineering and seismology.

Numerical results led to the development of a set of synthetic asperity distributions with uniform and lognormal distribution statistics based on the experimental asperity distribution. By varying the log-standard deviation for three cases, the tangential stiffness of the interface was observed to systematically increase and the energy dissipated decreased as the width of the asperity size distribution decreased. An end-member case with uniform asperity sizes exhibited the highest stiffness but also the highest energy dissipation. These results were in agreement with the proportionality relationships between tangential stiffness and variation in asperity radii recently proposed. While this frictional formulation is typically used to study engineering applications, the ability of the model to asses oscillatory behavior of asperities on faults may bode well for an understanding of the newly observed earthquake phenomena that appear to be triggered through vibrational forcings.

Notes

Acknowledgements

Funding for this research was provided by the National Science Foundation Grant CMMI-1131582 to the University of California, the Jane Lewis Fellowship (University of California, Berkeley) and the National Science and Engineering Research Council of Canada (PGSD3-391943-2010) provided to P. A. Selvadurai. J. Parker would also like to thank the National Defense Science and Engineering Graduate Fellowship (NDSEG) Program fellowship awarded by the Department of Defense (DoD).

References

1. ABAQUS/CAE user's manual: version 6.4. Pawtucket, RI: ABAQUS (2003)Google Scholar

2. Abercrombie RE, Rice JR (2005) Can observations of earthquake scaling constrain slip weakening? Geophys J Int 162(2):406–424. doi: 10.1111/j.1365-246X.2005.02579.xCrossRefGoogle Scholar

3. Aki K (1967) Scaling law of seismic spectrum. J Geophys Res 72(4):1217–1231CrossRefGoogle Scholar

4. Andrews DJ (1976) Rupture propagation with finite stress in antiplane strain. J Geophys Res 81(20):3575–3582. doi: 10.1029/JB081i020p03575CrossRefGoogle Scholar

5. Archard JF (1953) Contact and rubbing of flat surfaces. J Appl Phys 24(8):981–988. doi: 10.1063/1.1721448CrossRefGoogle Scholar

6. Archard JF (1957) Elastic deformation and the laws of friction. Proc R Soc Lond A Math Phys Eng Sci 243(1233):190–205. doi: 10.1098/rspa.1957.0214CrossRefGoogle Scholar

7. Archard JF (1961) Single contacts and multiple encounters. J Appl Geophys 32(8):1420–1425. doi: 10.1063/1.1728372Google Scholar

8. Ariyoshi K, Hori T, Ampuero JP, Kaneda Y, Matsuzawa T, Hino R (2009) Influence of interaction between small asperities on various types of slow earthquakes in a 3-D simulation for a subduction plate boundary. Godwana Res 16:534–544CrossRefGoogle Scholar

9. Ariyoshi K, Matsuzawa T, Ampuero JP, Nakata R, Hori T, Kaneda Y, Hino R, Hasegawa A (2012) Migration process of very low-frequency events based on a chain-reaction model and its application to the detection of preseismic slip for megathrust earthquakes. Earth Planets Space 64(8):693–702. doi: 10.5047/eps.2010.09.003CrossRefGoogle Scholar

10. Berthoude P, Baumberger T (1998) Shear stiffness of a solid solid multicontact interface. Proc R Soc Lond A 454(1974):1615–1634. doi: 10.1098/rspa.1998.0223CrossRefGoogle Scholar

11. Boitnott GN, Biegel RL, Scholz CH, Yoshioka N, Wang W (1992) Micromechanics of rock friction 2: quantitative modeling of initial friction with contact theory. J Geophys Res 97(B6):8965–8978CrossRefGoogle Scholar

12. Bouton GD (2014) CorelDRAW X7: the official guide, 11th edn. McGraw-Hill Education Group, New YorkGoogle Scholar

13. Brodsky EE, Lay T (2014) Recognizing foreshocks from the 1 April 2014 Chile earthquake. Science 344(6185):700–702. doi: 10.1126/science.1255202CrossRefGoogle Scholar

14. Brune JN (1970) Tectonic stress and spectra of seismic shear waves from earthquakes. J Geophys Res 75(26):4997–5009. doi: 10.1029/JB075i026p04997CrossRefGoogle Scholar

15. Cattaneo C (1938) Sul contatto di due corpi elastici: Distribuzione locale degli sforzi. Reconditi del Accademia Nazionale de Lincei 27:342–348, 434–436, 474–478Google Scholar

16. Ciavarella M (1998) The generalized Cattaneo partial slip plane contact problem. I—Theory. Int J Solids Struct 35(18):2349–2362. doi: 10.1016/S0020-7683(97)00154-6CrossRefGoogle Scholar

17. Ciavarella M (1998) The generalized Cattaneo partial slip plane contact problem. II—Examples. Int J Solids Struct 35(18):2363–2378. doi: 10.1016/S0020-7683(97)00155-8CrossRefGoogle Scholar

18. Davis RO, Selvadurai APS (1996) Elasticity and geomechanics. Cambridge University Press, CambridgeGoogle Scholar

19. Dieterich JH (1979) Modeling of rock friction: 1. Experimental results and constitutive equations. J Geophys Res 84(B5):2161–2168. doi: 10.1029/JB084iB05p02161CrossRefGoogle Scholar

20. Dieterich JH, Kilgore BD (1996) Implications of fault constitutive properties for earthquake prediction. Proc Nat Acad Sci USA 93(9):3787–3794CrossRefGoogle Scholar

21. Dini DD, Hills DA (2009) Frictional energy dissipation in a rough hertzian contact. Am Soc Mech Eng J Tribol 131(2):021401–021408Google Scholar

22. Dublanchet P, Bernard P, Favreau P (2013) Interactions and triggering in a 3-D rate-and-state asperity model. J Geophys Res 118:2225–2245. doi: 10.1002/jgrb.50187CrossRefGoogle Scholar

23. Greenwood JA, Williamson JBP (1966) Contact of nominally flat surfaces. Proc R Soc Lond A 295(1442):300–319. doi: 10.1098/rspa.1966.0242CrossRefGoogle Scholar

24. Griffith AA (1921) The phenomena of rupture and flow in solids. Philos Trans R Soc Lond A Math Phys Eng Sci 221(582–593):163–198. doi: 10.1098/rsta.1921.0006CrossRefGoogle Scholar

25. Hansen A, Schmittbuhl J, Batrouni GG, de Oliveira FA (2000) Normal stress distribution of rough surfaces in contact. Geophys Res Lett 27(22):3639–3642CrossRefGoogle Scholar

26. Hertz H (1882) On the contact of firm elastic bodies (in German: Ueber die berhrung fester elastischer krper). J Reine Angew Math 92:156–171Google Scholar

27. Houston H, Delbridge BG, Wech AG, Creager KC (2011) Rapid tremor reversals in Cascadia generated by a weakened plate interface. Nat Geosci 4:404–409CrossRefGoogle Scholar

28. Ida Y (1972) Cohesive force across the tip of a longitudinal-shear crack and griffith's specific surface energy. J Geophys Res 77(20):3796–3805. doi: 10.1029/JB077i020p03796CrossRefGoogle Scholar

29. Ida Y (1973) Stress concentration and unsteady propagation of longitudinal shear cracks. J Geophys Res 78(17):3418–3429. doi: 10.1029/JB078i017p03418CrossRefGoogle Scholar

30. Johnson KL (1985) Contact mechanics. Cambridge University Press, CambridgeCrossRefGoogle Scholar

31. Jones LM, Molnar P (1979) Some characteristics of foreshocks and their possible relationship to earthquake prediction and premonitory slip on faults. J Geophys Res 84(B7):3596–3608CrossRefGoogle Scholar

32. Kanamori H, Heaton TH (2000) Microscopic and macroscopic physics of earthquakes. In: Rundle JB, Turcotte DL, Klein W (eds) Geocomplexity and the physics of earthquakes. American Geophysical Union, Washington, DCGoogle Scholar

33. Kato A, Fukuda J, Kumazawa T, Nakagawa S (2016) Accelerated nucleation of the 2014 Iquique, Chile mw 8.2 earthquake. Sci Rep. doi: 10.1038/srep24792

34. Kato A, Igarashi T, Obara K (2014) Detection of a hidden Boso slow slip event immediately after the 2011 Mw 9.0 Tohoku-Oki earthquake, Japan. Geophys Res Lett 41(16):5868–5874. doi: 10.1002/2014GL061053CrossRefGoogle Scholar

35. Kostić S, Franović I, Perc M, Vasović N, Todorović K (2014) Triggered dynamics in a model of different fault creep regimes. Sci Rep 4:5401CrossRefGoogle Scholar

36. Li Q, Tullis TE, Goldsby D, Carpick RW (2011) Frictional ageing from interfacial bonding and the origins of rate and state friction. Nature 480:233–236. doi: 10.1038/nature10589CrossRefGoogle Scholar

37. MATLAB: Version 8.3 (R2014a). The MathWorks Inc., Natick, Massachusetts (2014)Google Scholar

38. McLaskey GC, Kilgore BD (2013) Foreshocks during the nucleation of stick-slip instability. J Geophys Res 118(6):2982–2997. doi: 10.1002/jgrb.50232CrossRefGoogle Scholar

39. McLaskey GC, Kilgore BD, Lockner DA, Beeler NM (2014) Laboratory generated M-6 earthquakes. Pure Appl Geophys. doi: 10.1007/s00024-013-0772-9Google Scholar

40. Medina S, Nowell D, Dini D (2013) Analytical and numerical models for tangential stiffness of rough elastic contacts. Tribol Lett 49(1):103–115. doi: 10.1007/s11249-012-0049-yCrossRefGoogle Scholar

41. Mindlin RD (1949) Compliance of elastic bodies in contact. J Appl Math 16:259–268Google Scholar

42. Noda H, Nakatani M, Hori T (2013) Large nucleation before large earthquakes is sometimes skipped due to cascade-Implications from a rate and state simulation of faults with hierarchical asperities. J Geophys Res Solid Earth 118(6):2924–2952. doi: 10.1002/jgrb.50211CrossRefGoogle Scholar

43. Nowell D, Dini D, Hills DA (2006) Recent developments in the understanding of fretting fatigue. Engineering Fracture Mechanics 73(2):207–222. doi: 10.1016/j.engfracmech.2005.01.013. http://www.sciencedirect.com/science/article/pii/S0013794405001803. Advanced Fracture Mechanincs for Life Safety Assessments

44. Obara K, Kato A (2016) Connecting slow earthquakes to huge earthquakes. Science 353(6296):253–257. doi: 10.1126/science.aaf1512CrossRefGoogle Scholar

45. Ohnaka M (1992) Earthquake source nucleation: a physical model for short-term precursors. Tectonophysics 211(1–4):149–178. doi: 10.1016/0040-1951(92)90057-DCrossRefGoogle Scholar

46. Ohnaka M (1993) Critical size of the nucleation zone of earthquake rupture inferred from immediate foreshock activity. J Phys Earth 41(1):45–56. doi: 10.4294/jpe1952.41.45CrossRefGoogle Scholar

47. Ohnaka M, Shen LF (1999) Scaling of the shear rupture process from nucleation to dynamic propagation: implications of geometric irregularity of the rupturing surfaces. J Geophys Res 104(B1):817–844. doi: 10.1029/1998JB900007CrossRefGoogle Scholar

48. Ohnaka M, Yamashita T (1989) A cohesive zone model for dynamic shear faulting based on experimentally inferred constitutive relation and strong motion source parameters. J Geophys Res Solid Earth 94(B4):4089–4104. doi: 10.1029/JB094iB04p04089CrossRefGoogle Scholar

49. Okubo PG, Dieterich JH (1984) Effects of physical fault properties on frictional instabilities produced on simulated faults. J Geophys Res 89(B7):5817–5827. doi: 10.1029/JB089iB07p05817CrossRefGoogle Scholar

50. Paggi M, Pohrt R, Popov VL (2014) Partial-slip frictional response of rough surfaces. Sci Rep 4:5178. doi: 10.1038/srep05178CrossRefGoogle Scholar

51. Peng Z, Vidale JE, Wech AG, Nadeau RM, Creager KC (2009) Remote triggering of tremor along the San Andreas fault in central California. J Geophys Res Solid Earth. doi: 10.1029/2008JB006049.B00A06Google Scholar

52. Persson BNJ (1999) Sliding friction. Surf Sci Rep 33:89–119CrossRefGoogle Scholar

53. Persson BNJ (2006) Contact mechanics for randomly rough surfaces. Surf Sci Rep 61(4):201–227. doi: 10.1016/j.surfrep.2006.04.001CrossRefGoogle Scholar

54. Peyrat S, Olsen KB, Madariaga R (2004) Which dynamic rupture parameters can be estimated from strong ground motion and geodetic data?. Birkhäuser Basel, Basel, pp 2155–2169Google Scholar

55. Rice JR, Ruina A (1983) Stability of steady frictional slipping. Am Soc Mech Eng 50(2):343–349. doi: 10.1115/1.3167042Google Scholar

56. Rubin AM, Ampuero JP (2005) Earthquake nucleation on (aging) rate and state faults. J Geophys Res Solid Earth. doi: 10.1029/2005JB003686Google Scholar

57. Ruina A (1983) Slip instability and state variable friction laws. J Geophys Res 88(B12):10359–10370. doi: 10.1029/JB088iB12p10359CrossRefGoogle Scholar

58. Saltiel S, Bonner BP, Ajo-Franklin JB (2017) Strain-dependent partial slip on rock fractures under seismic-frequency torsion. Geophys Res Lett 44(10):4756–4764. doi: 10.1002/2017GL073108.2017GL073108CrossRefGoogle Scholar

59. Saltiel S, Selvadurai PA, Bonner BP, Glaser SD, Ajo-Franklin JB (2017) Experimental development of low-frequency shear modulus and attenuation measurements in mated rock fractures: Shear mechanics due to asperity contact area changes with normal stress. Geophysics 82(2):M19–M36CrossRefGoogle Scholar

60. Schmittbuhl J, Chambon G, Hansen A, Bouchon M (2006) Are stress distributions along faults the signature of asperity squeeze? Geophys Res Lett 33(13):L13,307. doi: 10.1029/2006GL025952CrossRefGoogle Scholar

61. Scholz CH (2002) The mechanics of earthquakes and faulting, 2nd edn. Cambridge University Press, CambridgeCrossRefGoogle Scholar

62. Selvadurai PA (2015) Laboratory studies of frictional sliding and the implications of precursory seismicity. Ph.D. thesis, University of California, BerkeleyGoogle Scholar

63. Selvadurai PA, Glaser SD (2014) Insights into dynamic asperity failure in the laboratory. In: 48th US rock mechanics/geomechanics symposium. Minneapolis, MN, USA, pp ARMA 14–143Google Scholar

64. Selvadurai PA, Glaser SD (2015) Laboratory-developed contact models controlling instability on frictional faults. J Geophys Res 120(6):4208–4236. doi: 10.1002/2014JB011690CrossRefGoogle Scholar

65. Selvadurai PA, Glaser SD (2015) Novel monitoring techniques for characterizing frictional interfaces in the laboratory. Sensors 15(5):9791–9814. doi: 10.3390/s150509791CrossRefGoogle Scholar

66. Selvadurai PA, Glaser SD (2017) Asperity generation and its relationship to seismicity on a planar fault: a laboratory simulation. Geophys J Int 208:10091025. doi: 10.1093/gji/ggw439CrossRefGoogle Scholar

67. Selvadurai P, Edwards B, Tormann T, Wiemer S, Glaser S (2017) Characteristics of seismicity on worn faults—source dimensions of frictional precursory seismicity controlled by fault roughness (**under review**)Google Scholar

68. Svetlizky I, Fineberg J (2014) Classical shear cracks drive the onset of dry frictional motion. Nature 509:205–209CrossRefGoogle Scholar

69. Timoshenko SP, Goodier JN (1970) Theory of elasticity. McGraw-Hill, New YorkGoogle Scholar

70. Udías A, Madariaga R, Bufron E (2014) Source mechanisms of earthquakes: theory and practice. Cambridge University Press, CambridgeCrossRefGoogle Scholar

71. Wang W, Scholz CH (1994) Wear processes during frictional sliding of rock: a theoretical and experimental study. J Geophys Res Solid Earth 99(B4):6789–6799. doi: 10.1029/93JB02875CrossRefGoogle Scholar

72. Wang W, Scholz CH (1995) Micromechanics of rock friction: 3. Quantitative modeling of base friction. J Geophys Res Solid Earth 100(B3):4243–4247. doi: 10.1029/94JB02915CrossRefGoogle Scholar

73. Yoshimitsu N, Kawakata H, Takahashi N (2014) Magnitude-7 level earthquakes: a new lower limit of self-similarity in seismic scaling relationships. Geophys Res Lett 41(13):4495–4502. doi: 10.1002/2014GL060306.2014GL060306CrossRefGoogle Scholar

74. Yoshioka N (1997) A review of the micromechanical approach to the physics of contacting surfaces. Tectonophysics 277:29–40. doi: 10.1016/S0040-1951(97)00076-0CrossRefGoogle Scholar

75. Yoshioka N, Iwasa K (1996) The characteristic displacement in rate and state-dependent friction from a micromechanical point of view. Pure Appl Geophys 147(3):433–453. doi: 10.1007/BF00878837CrossRefGoogle Scholar

76. Yoshioka N, Scholz CH (1989) Elastic properties of contacting surfaces under normal and shear loads: 2. Comparison of theory with experiment. J Geophys Res Solid Earth 94(B12):17691–17700. doi: 10.1029/JB094iB12p17691CrossRefGoogle Scholar